ACS APPLIED POLYMER MATERIALS

Article

Cite This: ACS Appl. Polym. Mater. 2019, 1, 1559−1567

pubs.acs.org/acsapm

Simultaneous in Situ X-ray Scattering and Infrared Imaging of Polymer Extrusion in Additive Manufacturing

Yuval Shmueli,*[,†] Jiaolong Jiang,[†] Yuchen Zhou,[†] Yuan Xue,[†] Chung-Chueh Chang,[‡] Guangcui Yuan,[§] Sushil K. Satija,[§] Sungsik Lee,[∥] Chang-Yong Nam,[⊥] Taejin Kim,[†] Gad Marom,[#] Dilip Gersappe,[†] and Miriam H. Rafailovich[†]

[†]Department of Materials Science and Chemical Engineering, Stony Brook University, Stony Brook, New York 11794, United States

[‡]ThINC Facility, Advanced Energy Center, Stony Brook, New York 11794, United States

[§]Center for Neutron Research, National Institute of Standards and Technology, Gaithersburg, Maryland 20899, United States

[∥]X-ray Science Division, Argonne National Laboratory, Argonne, Illinois 60349, United States

[⊥]Center for Functional Nanomaterials, Brookhaven National Laboratory, Upton, New York 11973, United States

[#]Casali Institute of Applied Chemistry, The Institute of Chemistry and the Center for Nanoscience and Nanotechnology, The Hebrew University of Jerusalem, Jerusalem 91904, Israel

Supporting Information

ABSTRACT: In situ wide-angle X-ray scattering together with infrared imaging was performed during three-dimensional material extrusion printing and correlated with the development of the crystalline structure and subsequent thermomechanical properties. Identical samples were printed with nozzle motion either along the short axis or the long axis. The short axis mode had higher thermal retention, which resulted in later onset of crystal structure. The longer time spent at temperatures between the glass transition and the melting point produced samples with higher degree of crystallinity but also significantly increased brittleness. The tracer diffusion coefficient $D(T)$, together with its temperature dependence, was measured using neutron reflectivity, and the total interdiffusion length between filaments was then calculated using $D(T)$ for each temperature point, as determined by the measured thermal profiles. This allowed us to define the time/temperature plane that yielded the minimum diffusion length ΔL that provides mechanical integrity of the printed features (ΔL less than the radius of gyration of the poly(L-lactide)). The model was probed by printing structures at four nozzle temperatures and measuring the time dependence of the thermal profiles at filaments in the horizontal and vertical positions. The data indicated that the thermal retention was anisotropic, where higher values were obtained in the horizontal plane. Mechanical measurements indicated large differential increases in the torsional strength, corresponding to the direction with increased thermal retention.

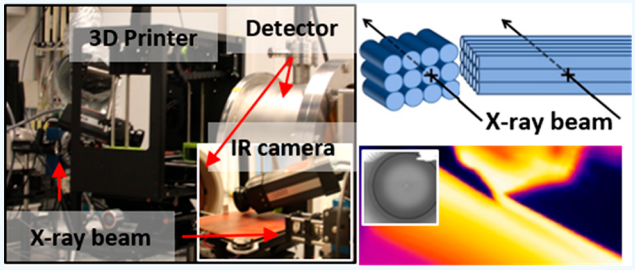

KEYWORDS: *additive manufacturing, in situ X-ray scattering, polylactic acid, interfacial diffusion, thermal imaging*

INTRODUCTION

Additive manufacturing, also known as 3D printing (3D = three-dimensional), is a widespread manufacturing technique being used in many industrial and academic areas.[1−4] 3D printing is a cost-effective technique in which one can make specific desired designs or products without the cost of molds preparation and materials excess. In 1992 S. S. Crump, founder of Stratasys Inc., developed the printing method of fused deposition modeling, which was recently named material extrusion (MatEx), in which thermoplastic polymer is being melted and extruded in certain shapes according to the user input file.[5] Since then, the MatEx printing method has become very common and popular due to its simplicity and relatively low cost.

The process of MatEx printing is rapid and occurs in nonequilibrium conditions. As such, to maintain high quality of products, all process aspects need to be studied in detail to be optimized. One of the main and crucial aspects is the fusion ("welding") dynamics between the deposited thermoplastic filaments. Fusion determines the interfacial characteristics between filaments and is directly correlated with the quality of the printed products and their mechanical properties. The fusion between filaments is controlled by polymer chain dynamics, which in turn is controlled by multiple factors such as temperature, glass transition (Tg), melting point (Tm), crystallinity, printing speed, and molecular weight. In contrast to bulk properties, this process is much harder to monitor, since it happens in rapid, nonequilibrium conditions on

Received: April 9, 2019
Accepted: May 13, 2019
Published: May 13, 2019

DOI: 10.1021/acsapm.9b00328
ACS Appl. Polym. Mater. 2019, 1, 1559−1567

micrometers to nanometers scale. Several groups studied fusion phenomena in thermoplastic polymers processing. Yang et al. first presented a model for thermoplastic welding under non-isothermal conditions,[6] where they concluded that maximal strength is achieved when a polymer chain reptates fully from its original "tube" in a time, $t \approx (1/T)^4$, known as the welding time, where T is the welding process temperature. Building on these concepts, C. McIlroy et al. presented a comprehensive theoretical model, which included the influence of temperature gradients, asymmetric deformation of the filaments under shear, as well a combination of Rouse and reptation dynamics, from which they concluded that the temperature profile generated during printing was key to establishment of the interface.[7] Q. Sun et al. was one of the first groups to measure the temperature profiles of extruded filaments.[8] They placed thermocouples on the nozzle next to the filament exit and below the printed shape in the printer base to determine the effects of the process parameters on the filament bonding. More recently J. Seppala et al. demonstrated the power of infrared spectroscopy to monitor spatial changes in the thermal profiles generated by the nozzle during MatEx printing as the polymer was deposited layer by layer.[9] N. G. Morales et al. studied the effect of temperature and cooling rate on the adhesion between deposited layers of acrylonitrile butadiene styrene (ABS) by adjusting the time frames between the depositions.[10] They showed the crucial effect of fast cooling on the decreasing adhesion between layers. C. Y. Lee et al. investigated the effect of the fan cooling on poly(L-lactide) (PLA) printing process for different printing configurations.[11] They demonstrated how the air flow, which affects the temperature at the nozzle area, can lead to higher printed shape quality when it is increased but reduces mechanical properties at the same time due to lower bonding between adjacent deposited filaments. They also show by infrared thermal imaging the higher temperature in a sample printed in short axis configuration.

These theoretical and experimental studies emphasized the importance of interfacial structure in determining the integrity of the printed structures. Several groups, therefore, intentionally modified the interfaces, including P. Levenhagen et al., who added a lower molecular weight fraction and demonstrated enhanced mechanical properties, which they attributed to faster migration of the lower molecular weight fraction to the interfaces.[12] A similar idea was also the basis of the core–shell filaments printed by F. Peng et al., where the outer filament was an elastomer with lower Tg and hence would diffuse faster.[13]

In this manuscript we focus on studying the in situ development of the crystalline structure and its dependence on the thermal profile. Crystalllinity is known to be an important factor affecting the interfacial structure, which can also have a profound effect on the interdiffusion at the filament interfaces. The crystal structures at the interface are much harder to predict, since they depend on the internal temperature, the temperature graidents, and the degree of crystallinity and orientation. To image the onset of crystalinity during the printing process we designed an open-structured printer, which could fit directly onto a synchrotron beam, and where the interfacial region could be simultaneously analyzed using X-ray scattering and infrared spectroscopy. Using this geometry we were able to accurately record the trasient thermal gradients, which are set up and dissipated during printing. In addition, as emphasized in a recent review by J. R. C. Dizon et al.,[14] multiple other factors such as printing orientaton and printing speed can influence the thermal profile. Here we show how the ability to record them simultaneously with data from X-ray scattering can reveal the corresponding crystalline orientation and hence the internal structure. Furthermore, since the degree of crystallinity for PLA is relatively small, we also utilized the thermal map, following the model of McIlroy et al.[7] to extract a diffusion length, and probed the extent to which interpenetration by at least a radius of gyration, Rg, factored into the final mechanical performance of the printed samples.

EXPERIMENTAL SECTION

Materials. PLA 4043D, average molecular weight, Mn = 67 kDa and polydispersity index (PDI) = 2.2 (measured by gas-phase chromatography (GPC)[15]) was purchased from NatureWorks LLC. Filaments (3.0 mm) for 3D MatEx printing were purchased from Matterhackers. Natural PLA grade was selected, which is based on the NatureWorks 4043D material and has similar viscosity [Figure S1, Supporting Information]. Silicon wafers, 5 mm thick, 7.5 cm in diameter, [1,0,0] orientation, single-side polished, were purchased from Wafer World. Polymer solutions for spin-casting thin films were made with Chloroform (Fisher Chemical, 99.9% purity).

Methods. *MatEx Printing.* Two MatEx printers were used. An Ultimaker Extended 2+ printer was used for ex situ printing using a 0.4 mm nozzle at a printing speed of 20 mm/s, which is a commonly used speed and was found optimized for the process. For experiments probing the effect of temperature, the nozzle temperature (Tn) was varied from 200 to 245 °C, while the bed was kept at room temperature. A Lulzbot Mini printer was used for the in situ measurements using a 0.5 mm nozzle with nozzle temperature of 230 °C and bed temperature of 60 °C at a printing speed of 20 mm/s.

The codes used to print the structures in this work were created by Matlab software and transformed into standard G-code for MatEx printing. The gap was adjusted for printing between the filaments to 0.4 mm to have 100% infill density.

The dimensions of the printed shapes were 2.5 × 15 × 200 mm^3, where the thickness was chosen to enable good transmittance and scattering of the X-rays. The shapes were printed using two orientations as shown in Figure 1. Figure 1a shows the sample

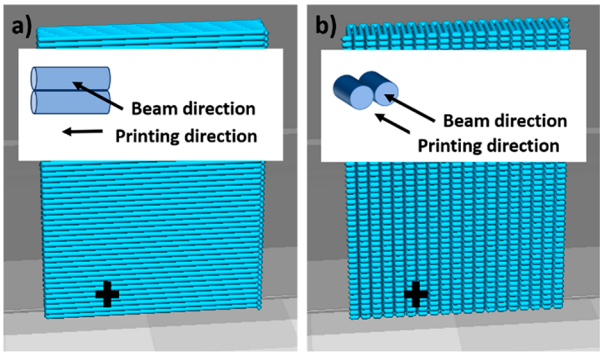

Figure 1. Two modes that were used for printing the structures relative to the X-ray beam direction. In situ WAXS measurements were performed where the structures were irradiated at the position marked with a plus sign (+). (a) Perpendicular orientation to beam. (b) Parallel orientation to beam.

where the shape was built by moving the print head along the long direction of the sample, and the motion of the head was perpendicular to the beam direction (marked with the arrow and the (+)), while Figure 1b shows the shape printed along the short direction of the sample, where the print head motion was parallel to the beam direction.

DOI: 10.1021/acsapm.9b00328
ACS Appl. Polym. Mater. 2019, 1, 1559–1567

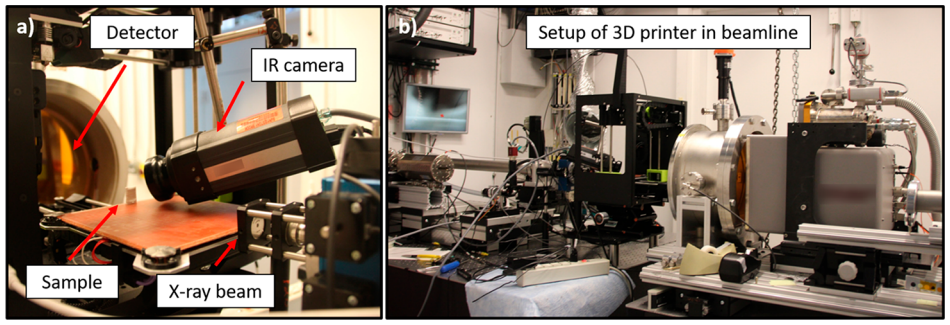

Figure 2. In situ experimental configuration for simultaneous WAXS analysis and thermal analysis of the 3D printing process. (a) Enlarged image showing placement of the IR thermal imaging camera and the X-ray detection system. (b) Placement of the printer relative to the beamline.

Wide-Angle X-ray Scattering (WAXS) of Single PLA Filaments. WAXS patterns of single PLA filaments were obtained on beamline 12BM at the Advanced Photon Source (APS) at Argonne National Laboratory. The beam energy was 14 keV with spot size of 500 μm, detector pixels size of 0.146 mm, and detector-to-sample distance of 243 mm.

In Situ WAXS and Thermal Imaging Measurements of Printing Process. Open-walls Lulzbot Mini MatEx printer was placed in beamline 12BM at the APS at Argonne National Laboratory. The beam energy was 16 keV with spot size of 500 μm, detector pixels size of 0.146 mm, and detector-to-sample distance of 567 mm. IR thermal camera (FLIR, A325sc) was fixed to monitor the temperature profile in the printed sample (Figure 2). X-ray scattering was done in two second intervals, and the scattering pattern represents the average of these two seconds.

Thermal imaging was recorded continuously. The beam location was fixed on the same position in the printed structure, and the scattering was measured while the printing was in process and layers were being deposited above. The impact on the temperature profiles by X-ray beam-induced thermal heating was investigated and found to be negligible [Figure S2, Supporting Information]. Analysis of the scattering data was done by xPolar software.

Neutron Reflectivity Measurements. Neutron reflectivity was used to measure the interdiffusion as a function of temperature. The experiments were done on the horizontal reflectometer at beamline NG7 with neutron wavelength of 0.475 nm at the National Institute for Standards and Technology (NIST), Center for Neutron Research (NCNR).

Sample Preparation for Neutron Reflectivity. Silicon wafers, 5 mm thick, were first cleaned of organic matter by boiling in a solution of 1:1:3 ammonium hydroxide, hydrogen peroxide, and deionized (DI) water for 15 min, followed by boiling for another 15 min in a solution of 1:1:3 sulfuric acid, hydrogen peroxide, and DI water, and rinsing in DI water. To remove the native oxide layer, the wafers were then hydrogen passivated by dipping in a 5% HF/DI water solution, followed by rinsing in DI water. A solution in chloroform of 90 wt % PLA, (NatureWorks 4043D), 10 wt % hydrogenated (H) poly(methyl methacrylate) (PMMA) (Mw: 50 600, PDI: 1.02, Polymer Source) was spun cast on the HF etched wafers at a speed of 3000 rpm. To remove solvent and relax tensions within the films, they were annealed at 120 °C for 2 h in vacuum. Another chloroform solution of 90 wt % PLA and 10 wt % deuterated (D) PMMA (Mw: 76 300 PDI: 1.09, Polymer Source) was spun cast on other HF etched wafer. Bilayer structures were fabricated by floating the D-PMMA/PLA film on the surface of a DI water bath and depositing it in a slow and controlled manner on the spun cast H-PMMA film. The bilayer samples were then dried in vacuum at room temperature for 24 h.

Bilayer samples of PLA/PMMA:PLA/D-PMMA were annealed for short times to simulate the diffusion of PLA in the printing process. The temperatures for annealing were chosen according to the thermal analysis result to be 140 °C, which is below the melting point but higher than the glass transition, 170 °C, which is above the melting point, and 200 °C, which is much above the melting point and closer to the measured polymer temperature at the exit of the nozzle.

The data were reduced by the "Reducts" and analyzed by neutron reflectivity web calculator[16] from the Center for Neutron Research at NIST and fitted using Matlab to a Fickian diffusion function to calculate the diffusion coefficients.

Temperature Profiles in the Extrusion and Printing Processes. Two setups were employed to measure the temperature profiles, using a high-resolution infrared thermal camera (FLIR, A325sc). A simple setup, involving a typical printer nozzle and filament roll, was used to determine the temperature profiles of the filament as it was being extruded as a function of the extrusion rate, nozzle diameter, and nozzle temperature (Figures S3–S5, Supporting Information). A second setup was assembled, where the thermal camera imaged the entire length of the nozzle travel of either the Ultimaker or the Lulzbot printers corresponding to an area encompassing four filaments. In this manner, fusion between filaments and the two-dimensional (2D) conduction pathway of the nozzle heat could be imaged.

Thermomechanical and SEM Characterization. Thermal analysis of the PLA was performed by the method of differential scanning calorimetry (DSC) with a heating rate of 10 °C/min (Q2000 TA Instruments). The thermal analysis results showed a glass transition temperature Tg = 60 °C and a melting temperature Tm = 150 °C (Figure S6, Supporting Information).

Torsion dynamic mechanical analysis (DMA) was performed in the Oscillation Amplitude mode at a frequency of 1 Hz, strain of 0.01–20%, and at a temperature of 100 °C on a DHR-2 rheometer (TA Instruments).

Thermal imaging was performed using a FLIR IR A325sc thermal camera with an imaging rate of 60 frames/sec and pixel size of 100 μm. Scanning electron microscopy (SEM) was performed using an LEO1550 Zeiss microscope. Cross-section samples for SEM imaging were prepared by cutting with an ultramicrotome to prevent flow of the polymer chains and to preserve the inner printed morphology.

RESULTS AND DISCUSSION

Evolution of Crystallinity during Printing. *Wide-Angle X-ray Scattering of Single Filaments.* We first characterized the commercial PLA filament, as received, before heating or extrusion from the printer nozzle. The WAXS spectra are shown in Figure S7 (Supporting Information), from which we can see that the as-received filament is amorphous, in agreement with the DSC data, which indicated a degree of crystallinity below 0.1%.

In Situ Simultaneous Wide-Angle X-ray Scattering (WAXS) with Thermal Imaging. To see the evolution of the crystalline structure together with the temperature dissipation during the MatEx printing process, simultaneous WAXS and thermal infrared spectra were obtained while the printer was in operation, and the results correlated with other material properties obtained with complementary imaging techniques. Two identical rectangular structures, 2.5 mm thick, 15 mm wide, and 200 mm high, were printed with the same printing

DOI: 10.1021/acsapm.9b00328
ACS Appl. Polym. Mater. 2019, 1, 1559–1567

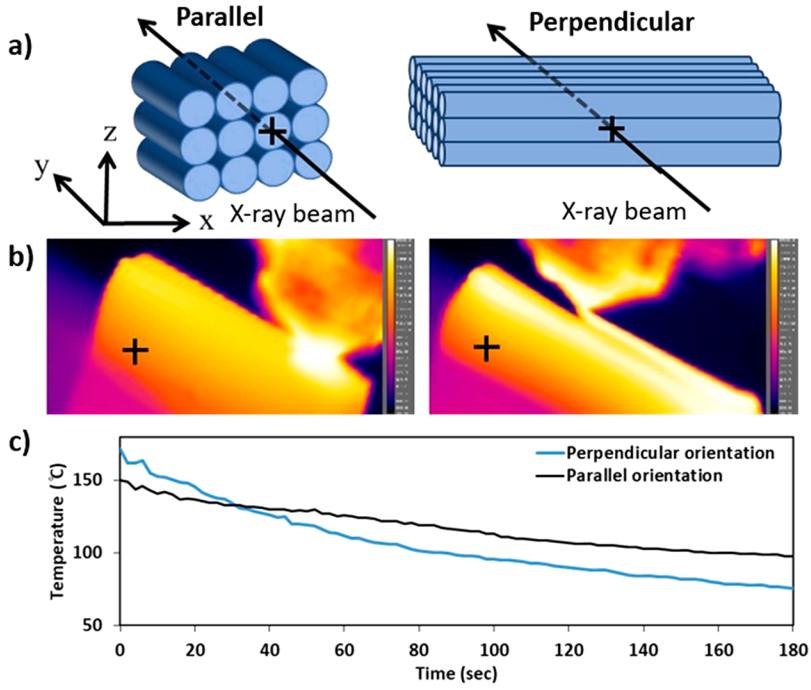

Figure 3. (a) Schematic illustration of the two printing orientations relative to the beam direction. (b) Typical thermal images of in situ printing process and sketches of the filaments−X-ray beam interaction: (left) parallel to beam and (right) perpendicular to beam. (c) Temperature change as a function of the printing orientation.

speed. As shown in Figure 1, one structure was built up with the nozzle traveling along the short axis, parallel to the X-ray beam, and a second structure was built with the nozzle traveling along the long axis, perpendicular to the X-ray beam direction. An expanded view of two types of structures are illustrated in Figure 3a, where the large (+) marks the position of the beam, and the arrow is along the beam direction.

The infrared camera was focused to image the entire printing area. A typical thermal image of the nozzle and the extruding filament for both orientations is shown in Figure 3b. In Figure 3c we plot the temperature profiles measured on the spot, designated by the (+) in Figure 3a, for printing in the two directions, after an initial three layers were printed to ensure the printing process had stabilized.

From the figure we see that cooling occurs exponentially with time for both orientations, reaching below the melting point, Tm ≈ 150 °C, within seconds. Initially the parallel orientation is observed to cool faster than the perpendicular orientation, which can be explained in terms of the proximity of the nozzle to the point of interest, (+). After ∼35 s, the curves cross over, with the parallel structure cooling at a significantly slower rate. The cooling rate of the structures involves a competition between radiative heat loss from the filament surfaces with heat input from the moving nozzle. Initially, the thermal profiles at the (+) are dominated by the proximity of the nozzle. In the parallel orientation, the nozzle moves along the filament axis during deposition, crossing the measured spot only once per deposited layer, while in the parallel orientation the nozzle crosses five times during deposition of the same layer. Hence the temperature at the spot is higher. After ∼30 s, seven layers were deposited above the observation point, moving the nozzle further away such that its thermal influence decreases, and the heat loss from the perpendicular orientation becomes higher due to the larger exposed area. Hence the rate of heat loss is significantly faster in the perpendicular orientation than in the parallel one. From the figure we can see that the temperature in the perpendicular orientation dips below the glass transition, Tg = 60 °C, within the next 2 min, while the temperature in the parallel orientation remains above Tg, for at least the next 3 min, allowing more time for crystallization to occur.

The WAXS spectra corresponding to the position designated with the (+) on both structures taken as a function of time during the printing process are shown in Figure 4a. From the figure we can see that initially the polymer is amorphous for both orientations. Two rings corresponding to the (200/110) and (203) planes of PLA α-phase[17,18] begin to appear indicating onset of crystallization. The peaks become sharper with increasing time, as the polymer continues to crystallize and the degree of crystallinity increases. The rings appear when the temperature is ∼120 °C, which occurs after only 70 s for perpendicular orientation and 96 s for the parallel orientation. In Figure 4b we plot a one-dimensional (1D) cross section of the 2D patterns, where we can see the amplitude of the two peaks corresponding to the crystallinity grows with increasing time. Fitting the peaks and integrating by using xPolar analysis software we can estimate the change in degree of crystallinity with time, which is plotted in Figure 4c. From the figure we can see that the perpendicular orientation reaches a plateau at ∼1.5%, while the parallel orientation achieves a value of 4.2% and is still increasing after 160 s. Analysis of the crystallization curves shows a simple relationship between the two orientations, where the larger overall heat retention, which occurs when the printing along the short axis orientation, delays the time for the onset of crystallization, but crystallization occurs at higher temperatures and for longer times, resulting in a significantly higher degree of crystallization.

Rheological Response. In Figure 5 we plot the modulus as a function of radial strain, where we can see that the sample

DOI: 10.1021/acsapm.9b00328
ACS Appl. Polym. Mater. 2019, 1, 1559−1567

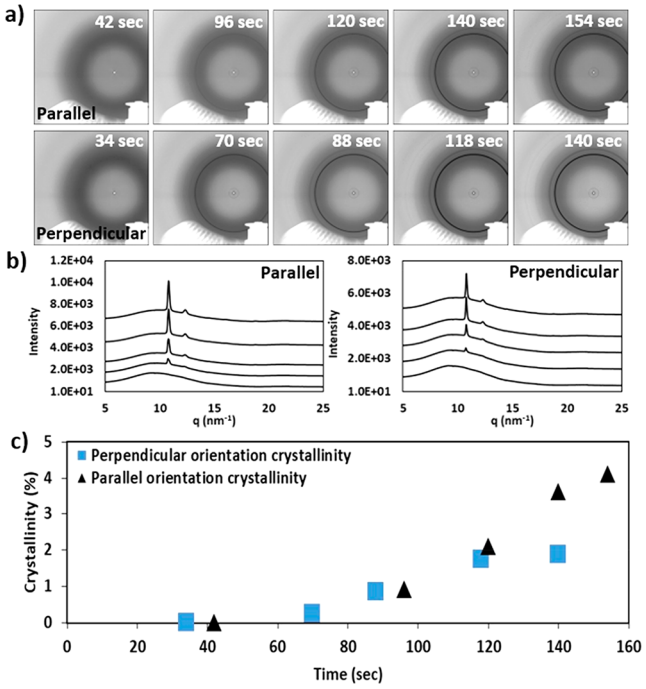

Figure 4. (a) 2D WAXS patterns obtained as a function of time from the location marked with the (+) in Figure 1 above, at the positions (top) parallel to beam and (bottom) perpendicular to beam. (b) Evolution of the crystalline structure in 1D sections corresponding to the 2D images from Figure 1a (left) parallel to beam and (right) perpendicular to beam. (c) Percentage of crystallinity in the samples, as a function of time, calculated from the WAXS curves in Figure 1b in the parallel (▲) and perpendicular (■) orientations.

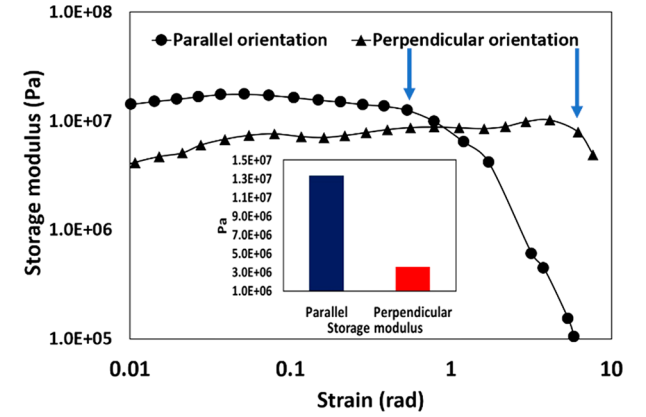

Figure 5. Storage modulus vs applied radial strain for samples printed in the parallel and perpendicular orientations. Arrows mark the break points for each sample. (inset) Zero shear modulus for samples printed in the two orientations.

printed along the parallel orientation is fairly insensitive to strain, while the sample printed in the perpendicular orientation undergoes strain hardening, asymptotically reaching the modulus of the parallel sample, as the higher temperatures allow for longer periods for stress relaxation induced by the crystallization process. The lack of strain hardening observed in these samples is also consistent with fewer defects in the material and increased ductility.[19,20] On the one hand, the inset shows the modulii at zero strain was nearly 4 times higher for the samples printed along the parallel orientation relative to the samples printed along the perpendicular orientation. On the other hand, the parallel sample breaks or delaminates at one-tenth of the strain that causes delamination of the perpendicular sample. This is consistent with increased crystallinity of the parallel sample, which increases the modulus, but it can also decrease ductility. The perpendicular sample though can withstand an order of magnitude larger strain, since as previously observed by multiple groups,[21−24] when the stress is applied along the filament direction the structure is much more resistant to delamination, as the force is absorbed by the filament. When the strain is applied along the interface between layers, delamination occurs easily.

Dependence of Filament Fusion on Nozzle Temperature. *Estimation of Diffusion Coefficient.* The improved mechanical properties observed in the parallel orientation may also be due to improved interpenetration between filaments. To achieve proper welding, polymer chains must diffuse and entangle with other chains at the filament interfaces. Entanglements are established when the chain emerges from its tube, reptating a distance equivalent to its radius of gyration Rg,[7,25] which for PLA of Mn = 60 000 was measured to be Rg ≈ 30 nm.[26]

In the case of crystalline polymers, the onset of crystalline organization at $T < Tm$, even for temperatures above Tg, will hinder interpenetration of chains across interfaces. Since the degree of crystallinity for the PLA filaments used here is relatively low (less than 5%) significant interdiffusion can occur in the interval $Tn > T > Tg$. During printing with fused filament fabrication, the temperature at the interfaces is continuously changing, and hence to determine the interpenetration depth between filaments, both the temperature-dependent self-diffusion coefficient and the time-dependent spatially resolved thermal profile must be determined.

The self-diffusion coefficient in a polymer melt can be measured using neutron reflectivity, where the interfacial broadening between two segments of a polymer bilayer films is measured as a function of time and temperature.[27] Deuteration of a small fraction of the chains is usually employed to obtain contrast for neutron scattering. Deuterated PLA chains though are very difficult to obtain. We therefore chose to use tracer amounts of PMMA, whose molecular weight and viscosity were similar to that of the PLA [Figure S8, Supporting Information], and since PMMA is completely miscible in PLA, no agglomeration would occur.[28] Bilayer samples were made, where the top and bottom layers were composed of PLA films containing 10% deuterated and hydrogenated PMMA, respectively. Neutron reflectivity was then used to measure the interfacial broadening between samples annealed at different temperatures [Figure 6a−c]. Three time points were collected at each temperature, and the interfacial width was plotted versus the square root of the time, $t^{1/2}$, as shown in Figure 6d. The tracer diffusion coefficient D was then obtained at each temperature using the relationship for the penetration depth ΔX for Fickian diffusion.

$$\Delta X = \sqrt{4Dt} \tag{1}$$

The diffusion coefficients $D(T)$ are tabulated in Table S1 [Supporting Information] as a function of temperature, where the data was fit to the Williams−Landel−Ferry (WLF) general equation for polymers diffusion,[17] where A and C are general parameters describing the materials properties of the material.

$$\ln D(T) \approx C + A(T - Tg) \tag{2}$$

DOI: 10.1021/acsapm.9b00328
ACS Appl. Polym. Mater. 2019, 1, 1559−1567

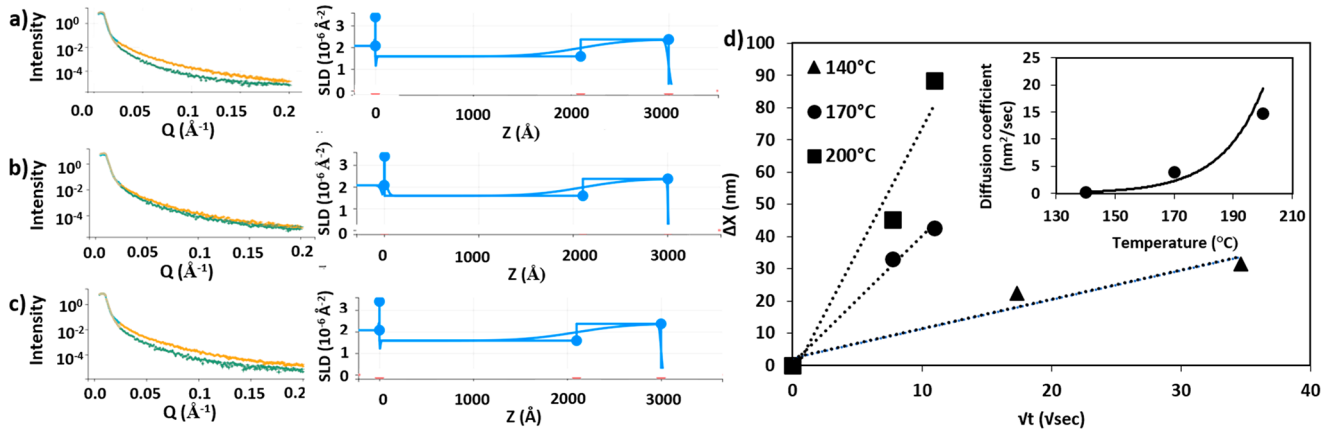

Figure 6. Representative neutron reflectivity: scattering intensity vs Q for as-cast films (gold) and annealed films (blue) and the scattering length density used to fit the data from both as-cast and annealed samples. (a) 140 °C for 5 min. (b) 170 °C for 1 min. (c) 200 °C for 1 min. (d) Interlayer diffusion ΔX vs $t^{1/2}$ at 140, 170, and 200 °C. (inset) Temperature dependence of the diffusion coefficients. Solid line: least-square fit to WLF equation.

where Tg = 60 °C, to obtain the following equation for the tracer diffusion in our system:

$$\ln D(T) \approx -43.7 + 0.071(T - Tg) \quad (3)$$

Substituting the expression for $D(T)$ back into eq 1 we get a general equation for diffusion length as a function of time and temperature.

$$\Delta X(T, t) = \sqrt{4 \times 10^{-19}(e^{0.071T})t} \quad (4)$$

$\Delta X(T,t)$ is plotted as a function of annealing time and temperature in Figure 7, together with the horizontal plane

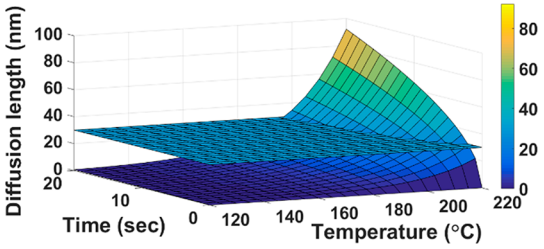

Figure 7. Diffusion length as a function of time and temperature for PLA calculated from eq 4. The plane at Rg = 30 nm marks the diffusion length required to entangle across the interface.

corresponding to Rg. To achieve adequate strength within a printed material the interdiffusion distance between filaments should be at least Rg, for entanglements to be established between adjacent filaments. From the position of the plane corresponding to Rg we can see that sample temperatures in excess of 200 °C, for time intervals that are temperature-dependent, are required to diffuse a distance of Rg before cooling of the sample has occurred. Therefore, the actual diffusion of chains during the printing process occurs mostly in the temperature interval between the nozzle temperature, T_1 = Tn, and the glass transition, T_2 = Tg, where chain motion is arrested. The total diffusion length L becomes a discrete sum of the distance traveled $\Delta X_i(T_i, t)$, $L = \sum_{T^1}^{T^2} \Delta X_i$, in constant time intervals, where the temperature at a given time following the onset of the printing is determined from the actual profiles measured during the printing process, which related the temperature and the time.

The Dependence of Filament Fusion on Nozzle Temperature. To determine the influence of the nozzle temperature and printing orientation on filament fusion, a construct was printed along the short orientation, with dimensions of 30 × 7 mm^2 and a thickness of 1.5 mm using four different nozzle temperatures. The temperature dissipation profile was then recorded as a function of time at the location of the adjacent filaments in the vertical and horizontal directions, as illustrated in Figure 8a. A typical thermal image is presented in Figure 8a. The distribution of temperatures across the four filament regions was then recorded as a function of time for different nozzle temperatures. The temperature profiles between adjacent horizontal and vertical filaments are plotted in Figure 8b,d as a function of time, from which we can see that a rapid decrease in temperature occurs within fractions of a second. The rate of decrease though varies significantly with filament position (horizontal or vertical) and nozzle temperature. The solid lines in the figure are fits to the data with an exponential function, $T(t) = ae^{-bt} + c$, where the coefficients a, b, and c are tabulated for each nozzle temperature and orientation in Table S2 (Supporting Information). Using these profiles, together with the neutron reflectivity results (Figure 6b and Table S1), we can now calculate $D(T)$ and substitute into the expression of ΔX, integrated over time intervals of 1/60 of a second (limited by the infrared instrumental resolution). The total diffusion length is then obtained by summation of ΔX within the temperature interval, Tn > T > Tg, where chain diffusion is assumed to be insignificant below Tg. The values of ΔL for the horizontal and vertical positions are plotted for each nozzle temperature in Figure 8c, together with Rg for PLA ≈ 30 nm.[26] From the figure we can see that the interdiffusion in the horizontal direction is on the order of Rg or higher when the nozzle temperature exceeds 215 °C, while the interdiffusion in the vertical direction approaches closer to Rg only at a nozzle temperature of 245 °C. Hence the printed structures achieve a sheetlike consistency, where delamination can occur along planes parallel to the surface at 215 °C < T < 245 °C.

The internal structure of the samples is also reflected in the mechanical properties. Torsional DMA was applied to the samples printed at different nozzle temperatures to experimentally examine the interdiffusion and the estimated diffusion coefficients. The modulii were measured as a function of radial strain amplitude (Figure 9a), where the maximal

DOI: 10.1021/acsapm.9b00328
ACS Appl. Polym. Mater. 2019, 1, 1559−1567

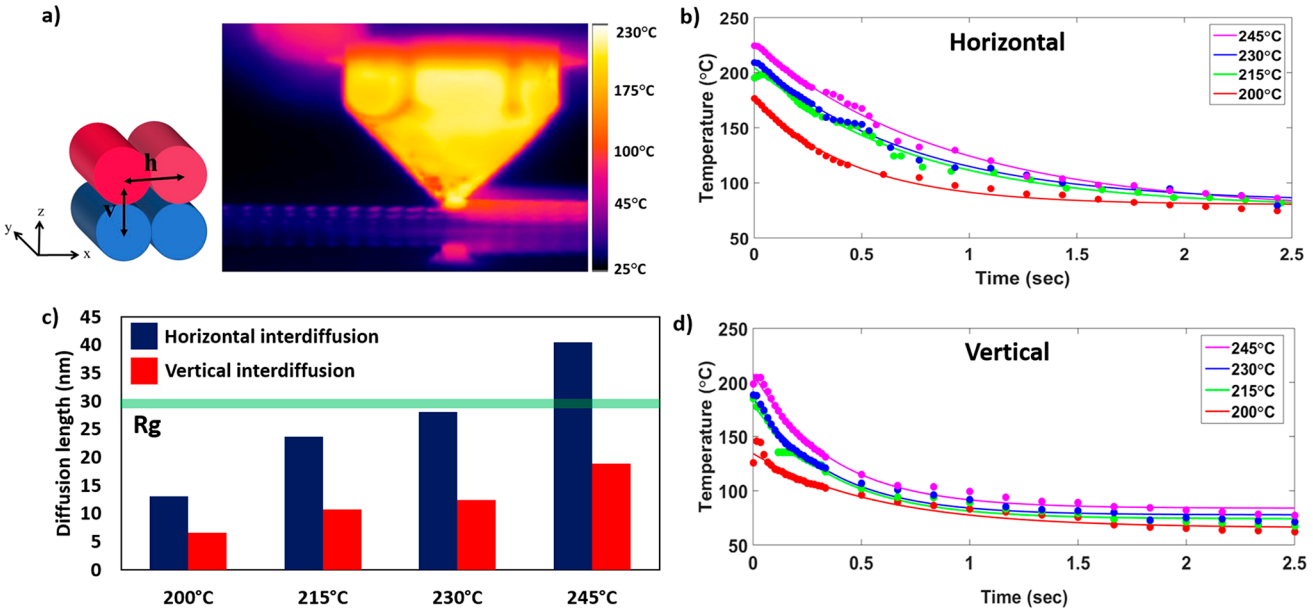

Figure 8. (a) (left) Schematic description of the matrix that was used for thermal analysis between adjacent filaments. (right) Thermal images of the printing process. (b) Temperature measured from deposition time between adjacent horizontal filaments as a function of time. (c) Total diffusion length between adjacent horizontal filaments as a function of nozzle temperature. (d) Temperature measured from deposition time between adjacent vertical filaments as a function of time.

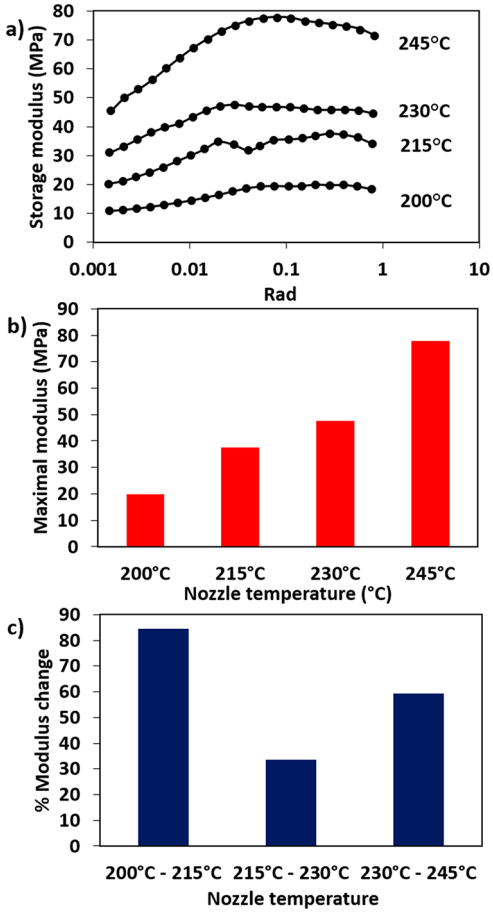

Figure 9. (a) Torsion DMA results of sample printed at nozzle temperatures of 200, 215, 230, and 245 °C. (b) Maximal modulus measured for each nozzle temperature. (c) Percentages of modulus change between the samples printed at the different nozzle temperatures.

values are plotted in Figure 9b. From the figure we can see that, even though the strain at break is similar for all samples, the storage modulii increase with increasing nozzle temperature. In Figure 9c we plot the differential increase in the modulii between samples printed with increasing nozzle temperature. From the figure we see that the largest differential occurs between the samples printed at 200 and 215 °C. In this case the internal structure change goes from completely unconnected fibers to fibers that are connected in the horizontal plane. Further increase in temperature from 215 to 230 °C slightly improved the horizontal interconnection but did not achieve vertical interconnection. In this case the differential increase in modulus is relatively small. The next increase occurs in the range between 230 and 245 °C, when the internal connectivity becomes spatially uniform, in both horizontal and vertical directions.

This can be seen in the SEM images of the cross sections taken from structures printed with nozzle temperatures of 200, 215, 230, and 245 °C (Figure 10). From the figure we can see that, for a nozzle temperature of 200 °C, incomplete welding occurs both in the horizontal and vertical directions. Increasing the temperature to 215 °C results in increased horizontal fusion, while minimal fusion is observed in the vertical direction. Fusion improves as the nozzle temperature increases further to 230 °C and, except for a few discrete exceptions at the filament edges, becomes nearly complete in all directions when the nozzle temperature is 245 °C. This observation is consistent with calculated diffusion lengths plotted in Figure 8c, which were derived from the measured thermal profiles of the filaments in the horizontal and vertical directions. From the figure we found that the diffusion length in the horizontal direction approached the radius of gyration, when fusion occurred, at a nozzle temperature of 230 °C, while the diffusion length in the vertical direction increased more slowly with nozzle temperature, exceeding Rg/2 only when the nozzle temperature was 245 °C.

DOI: 10.1021/acsapm.9b00328
ACS Appl. Polym. Mater. 2019, 1, 1559−1567

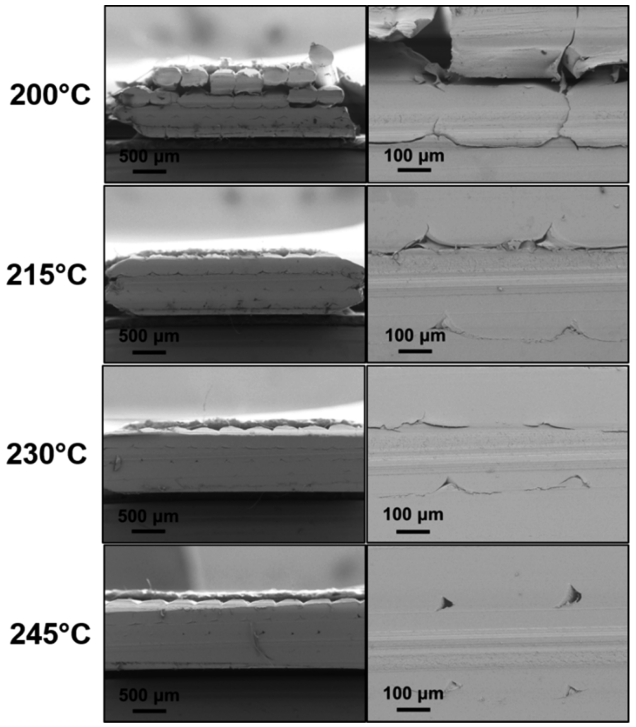

Figure 10. SEM images of the printed structures at nozzle temperatures of 200, 215, 230, and 245 °C.

CONCLUSIONS

In situ wide-angle X-ray scattering together with infrared thermal imaging was performed during 3D MatEx printing with a PLA filament. The results highlighted the importance of the temperature profiles during printing on the structure/property relationships of the samples. Printing along the short axis resulted in increased thermal retention and higher degrees of crystallinity and mechanical strength relative to samples printed along the long axis. The tracer diffusion coefficient was measured using neutron reflectivity and used to construct a model of the interdiffusion between filaments as a function of time and temperature. The thermal conduction between filaments in the vertical and horizontal direction was measured at four different nozzle temperatures, and the interdiffusion was determined by scanning electron microscopy. Good agreement was obtained between the theoretical predictions and the experimental results. The data showed that large differences exist within the structure during printing between adjacent filaments in the vertical and horizontal directions. Fusion, which was shown to occur when the diffusion length approached Rg of PLA, occurred first in the horizontal direction when the nozzle temperature exceeded 215 °C and in the vertical direction when the nozzle temperature reached 245 °C.

ASSOCIATED CONTENT

Supporting Information

The Supporting Information is available free of charge on the ACS Publications website at DOI: 10.1021/acsapm.9b00328.

Viscosity as a function of temperature for the PLA, the temperature profiles with and without the X-ray beam, the model for obtaining the temperature distribution following extrusion, DSC and WAXS patterns of the PLA filament before extrusion, calculation of the diffusion length at different nozzle temperatures (PDF)

AUTHOR INFORMATION

Corresponding Author

*E-mail: yuval.shmueli@stonybrook.edu.

ORCID

Yuval Shmueli: 0000-0002-0990-8440
Chang-Yong Nam: 0000-0002-9093-4063
Taejin Kim: 0000-0002-0096-303X

Author Contributions

The manuscript was written through contributions of all authors. Y.S., T.K., M.R., and G.M. led the research project and integrated all the elements in developing the research. J.J. and D.G. performed the modeling of temperature profile in the extrusion process. Y.Z., G.Y., and S.S. prepared the samples, assembled the experimental setup, and acquired and analyzed the data of the for neutron reflectivity. C.N. and S.L. installed the apparatus for in situ X-ray measurements and analyzed the X-ray data. C.C. and Y.X. performed and analyzed the mechanical measurements, and obtained and analyzed the SEM images.

Notes

The authors declare no competing financial interest.

ACKNOWLEDGMENTS

The authors acknowledge support from the National Science Foundation (Inspire Award No. 1344267). WAXS measurements were performed at the 12-BM beamline of the Advanced Photon Source at Argonne National Laboratory, a U.S. Department of Energy (DOE) Office of Science User Facility operated for the DOE Office of Science by Argonne National Laboratory under Contract No. DE-AC02-06CH11357. Thermomechanical characterization was performed at the Stony Brook Univ. ThINC core facility.

REFERENCES

(1) Fu, K.; Yao, Y. G.; Dai, J. Q.; Hu, L. B. Progress in 3D Printing of Carbon Materials for Energy-Related Applications. *Adv. Mater.* **2017**, *29*, 1603486.
(2) Gross, B. C.; Erkal, J. L.; Lockwood, S. Y.; Chen, C. P.; Spence, D. M. Evaluation of 3D Printing and Its Potential Impact on Biotechnology and the Chemical Sciences. *Anal. Chem.* **2014**, *86*, 3240−3253.
(3) Hofmann, M. 3D Printing Gets a Boost and Opportunities with Polymer Materials. *ACS Macro Lett.* **2014**, *3*, 382−386.
(4) Wendel, B.; Rietzel, D.; Kuhnlein, F.; Feulner, R.; Hulder, G.; Schmachtenberg, E. Additive Processing of Polymers. *Macromol. Mater. Eng.* **2008**, *293*, 799−809.
(5) Crump, S. S. Apparatues and Method for Creating Three-Dimensional Objects. U.S. Patent 5,121,329, Jun 9, 1992.
(6) Yang, F.; Pitchumani, R. Healing of thermoplastic polymers at an interface under nonisothermal conditions. *Macromolecules* **2002**, *35*, 3213−3224.
(7) McIlroy, C.; Olmsted, P. D. Disentanglement effects on welding behaviour of polymer melts during the fused-filament-fabrication method for additive manufacturing. *Polymer* **2017**, *123*, 376−391.
(8) Sun, Q.; Rizvi, G. M.; Bellehumeur, C. T.; Gu, P. Effect of processing conditions on the bonding quality of FDM polymer filaments. *Rapid Prototyping J.* **2008**, *14*, 72−80.
(9) Seppala, J. E.; Migler, K. D. Infrared thermography of welding zones produced by polymer extrusion additive manufacturing. *Addit. Manuf.* **2016**, *12*, 71−76.

DOI: 10.1021/acsapm.9b00328
ACS Appl. Polym. Mater. 2019, 1, 1559−1567

(10) Morales, N. G.; Fleck, T. J.; Rhoads, J. F. The effect of interlayer cooling on the mechanical properties of components printed via fused deposition. *Addit. Manuf.* **2018**, *24*, 243−248.
(11) Lee, C.-Y.; Liu, C.-Y. The influence of forced-air cooling on a 3D printed PLA part manufactured by fused filament fabrication. *Addit. Manuf.* **2019**, *25*, 196−203.
(12) Levenhagen, N. P.; Dadmun, M. D. Bimodal molecular weight samples improve the isotropy of 3D printed polymeric samples. *Polymer* **2017**, *122*, 232−241.
(13) Peng, F.; Zhao, Z. Y.; Xia, X. H.; Cakmak, M.; Vogt, B. D. Enhanced Impact Resistance of Three-Dimensional-Printed Parts with Structured Filaments. *ACS Appl. Mater. Interfaces* **2018**, *10*, 16087−16094.
(14) Dizon, J. R. C.; Espera, A. H.; Chen, Q. Y.; Advincula, R. C. O Mechanical characterization of 3D-printed polymers. *Addit. Manuf.* **2018**, *20*, 44−67.
(15) Meng, X. T.; Nguyen, N. A.; Tekinalp, H.; Lara-Curzio, E.; Ozcan, S. Supertough PLA-Silane Nanohybrids by in Situ Condensation and Grafting. *ACS Sustainable Chem. Eng.* **2018**, *6*, 1289−1298.
(16) Maranville, B. B. Interactive, Web-Based Calculator of Neutron and X-ray Reflectivity. *J. Res. Nat. Inst. Stand. Technol.* **2017**, *122*, 1.
(17) Pan, P.; Zhu, B.; Kai, W.; Dong, T.; Inoue, Y. Effect of crystallization temperature on crystal modifications and crystallization kinetics of poly(L-lactide). *J. Appl. Polym. Sci.* **2008**, *107*, 54−62.
(18) Yin, Y. G.; Zhang, X. Q.; Song, Y.; de Vos, S.; Wang, R. Y.; Joziasse, C. A. P.; Liu, G. M.; Wang, D. J. Effect of nucleating agents on the strain-induced crystallization of poly(L-lactide). *Polymer* **2015**, *65*, 223−232.
(19) Lim, C. T.; Tan, E. P. S.; Ng, S. Y. Effects of crystalline morphology on the tensile properties of electrospun polymer nanofibers. *Appl. Phys. Lett.* **2008**, *92*, 141908.
(20) Sarasua, J. R.; Arraiza, A. L.; Balerdi, P.; Maiza, I. Crystallinity and mechanical properties of optically pure polylactides and their blends. *Polym. Eng. Sci.* **2005**, *45*, 745−753.
(21) Ahn, S. H.; Montero, M.; Odell, D.; Roundy, S.; Wright, P. K. Anisotropic material properties of fused deposition modeling ABS. *Rapid Prototyping J.* **2002**, *8*, 248−257.
(22) Herrero, M.; Peng, F.; Nunez Carrero, K. C.; Merino, J. C.; Vogt, B. D. Renewable Nanocomposites for Additive Manufacturing Using Fused Filament Fabrication. *ACS Sustainable Chem. Eng.* **2018**, *6*, 12393−12402.
(23) Letcher, T.; Rankouhi, B.; Javadpour, S. In *Experimental Study of Mechanical Properties of Additively Manufactured ABS Plastic as a Function of Layer Parameters,* Proceedings of the ASME 2015 International Mechanical Engineering Congress and Exposition, Nov 13−19, 2015; ASME: Houston, Texas, 2015; IMECE2015-52634.
(24) Letcher, T.; Waytashek, M. In *Material Property Testing of 3D-Printed Specimen in PLA on an Entry-Level 3D Printer,* Proceedings of the ASME 2014 International Mechanical Engineering Congress and Exposition, Nov 14−20, 2014; ASME: Montreal, Quebec, Canada, 2014, IMECE2014-39379.
(25) Seppala, J. E.; Hoon Han, S. H.; Hillgartner, K. E.; Davis, C. S.; Migler, K. B. Weld formation during material extrusion additive manufacturing. *Soft Matter* **2017**, *13*, 6761−6769.
(26) Dorgan, J. R.; Janzen, J.; Knauss, D. M.; Hait, S. B.; Limoges, B. R.; Hutchinson, M. H. Fundamental solution and single-chain properties of polylactides. *J. Polym. Sci., Part B: Polym. Phys.* **2005**, *43*, 3100−3111.
(27) Imel, A. E.; Rostom, S.; Holley, W.; Baskaran, D.; Mays, J. W.; Dadmun, M. D. The tracer diffusion coefficient of soft nanoparticles in a linear polymer matrix. *RSC Adv.* **2017**, *7*, 15574−15581.
(28) Guo, Y. C.; Zuo, X. H.; Xue, Y.; Zhou, Y. C.; Yang, Z. H.; Chuang, Y. C.; Chang, C. C.; Yuan, G. C.; Satija, S. K.; Gersappe, D.; Rafailovich, M. H. Enhancing Impact Resistance of Polymer Blends via Self-Assembled Nanoscale Interfacial Structures. *Macromolecules* **2018**, *51*, 3897−3910.

DOI: 10.1021/acsapm.9b00328
ACS Appl. Polym. Mater. 2019, 1, 1559−1567